Co-published by
Institute of Fluid-Flow Machinery
Polish Academy of Sciences
Committee on Thermodynamics and Combustion
Polish Academy of Sciences

Copyright©2026 by the Authors under licence CC BY-NC-ND 4.0

http://www.imp.gda.pl/archives-of-thermodynamics/

Mixed convective chemically reacted hybrid nanofluid flowing over a non-isothermal/non-isosolutal cone/wedge with heat generation/absorption: A numerical study

Chegu Ramprasad[a], Chundru Maheswari[a*], Bhavanam Naga Lakshmi[b], Tadavarthi Madhu Mohan[c], Ravuri Mohana Ramana[d]

[a]Department of Mathematics, Vasireddy Venkatadri International Technological University, Nambur-522508, Andhra Pradesh, India
[b]Department of Mathematics, Vignan Nirula Institute of Technology for Women, Guntur-522009, Andhra Pradesh, India
[c]Department of Physics, Vasireddy Venkatadri International Technological University, Nambur-522508, Andhra Pradesh, India
[d]Department of Mathematics, Narasaraopeta Engineering College (Autonomous), Narasaraopet-522601, Andhra Pradesh, India
*Corresponding author email: cmaheswari2014@gmail.com

Received: 26.09.2025; revised: 08.07.2026; accepted: 21.07.2026

Abstract

The current study explores a numerical investigation of steady-state, two-dimensional, incompressible, laminar mixed convective flow of a chemically reactive hybrid nanofluid composed of $Al_2O_3 - H_2O$ over a vertical non- isothermal/isosolutal wedge and cone configurations, taking into account the impact of a heat absorption or generation parameter. Utilising similarity transformations, the set of governing equations was reduced to a set of ordinary differential equations. This model incorporates the conservation equations for energy, mass and momentum, which are solved numerically by using the BVP-5C method and the Runge-Kutta shooting technique in MATLAB. The influences of key factors on the flow fields, as well as on the mass and heat transmission rates, are analysed and presented through graphical and tabular formats. The outcome reveals that both solutal and thermal Grashof numbers display a comparable influence on the flow behaviour. As these parameters increase, an enhancement in the velocity profile is observed, whereas concentration and temperature distributions tend to decline. Additionally, an increase in the heat generation and thermal radiation parameters results in elevated temperature distributions for both wedge and cone geometries. In contrast, the chemical reaction factor contributes to a decrease in concentration distribution. The influence is more prominent in the wedge configuration than in the cone, where the profile exhibits an increasing behaviour, while the cone shows a stronger response in scenarios where the profile decreases. The mass and heat transmission rates corresponding to the key parameters are presented in tabulated form. The proposed model has been rigorously verified against previously reported data and demonstrates excellent agreement.

Keywords: Wedge/cone; Thermal/mass Grashof numbers; Heat generation/absorption parameter; Chemical reaction

Vol. 47(2026), No. 3, 99–110; doi: 10.24425/ather.2026.3659

Cite this manuscript as: Ramprasad, C., Maheswari, C., Naga Lakshmi, B., Mohan, T.M., & Ramana, R.M. (2026). Mixed convective chemically reacted hybrid nanofluid flowing over a non-isothermal/non-isosolutal cone/wedge with heat generation/absorption: A numerical study. *Archives of Thermodynamics*, 47(3), 99−110.

1. Introduction

Hybrid nanofluids are engineered by suspending a combination of two or more different nanoparticles within a conventional heat transmission medium such as water (H_2O), motor oil, organic solvents or biological fluids. When these nanoparticles are uniformly dispersed, the resulting fluid exhibits significantly improved thermal conductivity and superior heat transfer features. As an innovative class of working liquids, hybrid nanofluids have shown great promise in various engineering and scien-

Nomenclature

a, b – constants
Bi – Biot number
C – concentration, kg/m^3
C_f – skin friction coefficient
C_w – concentration at wall, kg/m^3
C_∞ – ambient concentration (kg/m^3)
D_{hnf} – diffusion coefficient, m^2/s
g – acceleration due to gravity, m/s^2
Gc – mass Grashof number
Gr – thermal Grashof number
h_f – convective heat transfer coefficient, W/(m^2 K)
k_{hnf} – thermal conductivity of hybrid nanofluid, W/(m K)
k^* – mean absorption coefficient, m^{-1}
l – characteristic length of cone/wedge, m
n – power index
Nu$_x$ – Nusselt number
Pr – Prandtl number
Q – heat generation/absorption parameter
q_r – heat flux, W/m^2
r – radius of the cone, m
Rc – chemical reaction parameter
Rd – thermal radiation
Re$_x$ – local Reynolds number
s_1 – wall temperature parameter
s_2 – wall concentration parameter
S – suction parameter
Sc – Schmidt number
Sh$_x$ – Sherwood number
T – temperature, K
T_w – temperature at wall, K
T_∞ – ambient temperature, K
u, v – velocity components along the x– and y–axis, m/s
u_w – stretching velocity, m/s

Greek symbols

α – half-angle
β_C – solutal expansion coefficient, K^{-1}
β_T – thermal expansion coefficient, K^{-1}
μ_{hnf} – dynamic viscosity of hybrid nanofluid, kg/(m s)
ρ_{hnf} – density of hybrid nanofluid, kg/m^3
$(\rho C_p)_{hnf}$ – heat capacity of hybrid nanofluids, J/(kg K)
σ^* – Stefan-Boltzmann constant, W/(m^2 K^4)
ϕ_1, ϕ_2 – Cu and Al_2O_3 nano particles volume fraction

Subscripts and Superscripts

∞ – free stream
f – fluid
hnf – hybrid nanofluids
w – at the wall/surface

Abbreviations and Acronyms

EG – ethylene glycol
MHD – magnetohydrodynamics
ODEs – ordinary differential equations

tific domains, including microfluidic systems, transportation technologies, biomedical applications, defence mechanisms, naval architecture and acoustic devices. Due to its extensive spectrum of applications in engineering and science, the investigation of fluid flow over different geometrical shapes such as vertical cones and wedges has attracted considerable interest from researchers. These flow configurations are crucial in various industrial and technological operations, including fibre production, advanced thermal aerodynamics, cooling of nuclear systems, surface modification, spray deposition techniques, and polymer fabrication. Consequently, a substantial amount of analytical and computational investigations have led to explore the flow behaviour of Newtonian as well as non-Newtonian fluids across such geometrical domains.

Dawar et al. [1] analysed the convective transport of Williamson's nanoliquid through wedge and cone geometries by employing convective boundary conditions. The flow was studied under varying thermal and solutal conditions that were not uniform across the surface. Kumar et al. [2] explored the laminar flow of a Newtonian composite nanofluid containing various nanoparticles embedded in a basic fluid, considering both temperature-dependent and exponentially changing spatial heat generation over an isothermal wedge. Yahaya et al. [3] examined steady-state hybrid nanoliquid flowing over a penetrable, non-isothermal wedge and cone, incorporating the influence of radiation and convective boundary conditions in their heat transmission analysis. Sushila et al. [4] analysed the heat transmission behaviour of TiO_2 – CuO/water hybrid nanoliquid flowing over both static and moving wedges, taking into account the effects of thermal radiation and magnetic field within a porous medium.

Mixed convection represents fluid flow in which both forced convection, caused by external pressure gradients, and free convection, resulting from buoyancy forces, act simultaneously. This type of flow plays a substantial role in an extensive array of applications, like low-speed heat exchangers, cooling of electronic components, crystal formation, underground cable networks, chemical manufacturing, lubrication systems, boilers, emergency cooling in nuclear reactors, solar thermal systems, defrosting mechanisms, atmospheric circulation, vehicle windshield demisters, and ocean currents. Ramzan et al. [5] inspected mixed convection flow of a ternary hybrid nanoliquid over wedge and cone geometries characterised by non-isothermal and non-isosolutal distributions. Reddy et al. [6] investigated mixed convective magnetohydrodynamics (MHD) radiative flow of a Williamson's nanoliquid over a wedge, including the influence of inner heat generation and binary chemical reactions. The mixed convective heat and mass transfer behaviour of a magneto-nanofluid over a moving vertical plate, including thermal radiation, was examined by Chandra Reddy et al. [7]. The influence of time-dependent MHD mixed convection on hybrid nanofluid flow past a nonlinearly stretching surface in a porous medium was investigated by Mathews and Hymavathi [8].

The study of fluid flow involving chemical reactions is vital due to its substantial influence on both environmental and industrial operations. Such reactions play a crucial role in a widespread range of applications, such as nuclear reactor systems,

atomic energy generation, plastic fabrication, cable insulation processes, and many other industrial sectors. Amit and Shalini [9] conducted a numerical study on the influence of a nonlinear chemically reacting MHD convective flow of Maxwell liquid over penetrable surfaces, including a vertical cone/wedge/plate. AL Garalleh [10] investigated the mixed convection flow of a ternary hybrid nanoliquid composed of TiO_2, Al_2O_3 and SiO_2 over a stretched/shrunk wedge, considering the combined influences of chemical reaction and activation energy. Arabi et al. [11] explored the convection behaviour of a Williamson hybrid nanoliquid flowing over wedge and cone geometries within a porous surface, considering various nanoparticle shapes and the effect of a chemical response.

The study of temperature distribution influenced by heat generation (absorption) in moving fluids plays a crucial role in numerous physical contexts, including chemical reaction processes and the behaviour of dissociating fluids. Numerous investigations in the literature focus on heat transmission in the laminar flow of viscous liquids. In some works, heat generation is modelled either as a constant or as a function of spatial coordinates, while others have incorporated the effects of frictional heating and fluid expansion. Vajravelu and Nayfeh [12] investigated MHD convection along cone and wedge surfaces, considering variable surface temperatures and the presence of inner heat absorption/generation. Rekha et al. [13] studied the influence of a uniform heat sink/source on the flow of an incompressible nanofluid over cone and wedge geometries within a permeable medium. The influence of heat generation and thermal radiation under exponentially varying temperature and concentration conditions was investigated by Chandra Reddy et al. [14]. The same authors, in [15], carried out a numerical investigation of free convection heat and mass transfer characteristics in a heat-producing magneto-nanofluid past a vertically moving plate. Mathews and Hymavathi [16] explored the effects of a magnetic field, viscous dissipation, thermal radiation and internal heat generation/absorption on flows involving metallic and oxide nanoparticles over a permeable stretching sheet.

By applying the MATLAB BVP4C boundary-value problem solver, Ali et al. [17,18] numerically explored the influence of various nanoparticle shape factors, including blade, brick, cylindrical, platelet, and spherical forms, on nanofluid flow characteristics, considering unsteady $SiO_2 – H_2O$ motion along a stretchable cylinder and steady EG–Cu flow over a fixed stretching surface under Joule heating effects. Shahzad et al. [19] examined the characteristics of axisymmetric liquid film flow and the associated heat transfer over a time-dependent radially stretching surface, accounting for the influence of an applied transverse magnetic field. Zaman et al. [20] explored the thermal behaviour of Williamson nanofluids incorporating upward-moving motile thermophilic microorganisms along wedge and cone surfaces and further enhanced their study by employing an artificial neural network to support the numerical findings. Ahmed et al. [21] investigated the effects of thermal radiation on chemically reactive MHD hybrid nanofluid flow over elastically deformable wedge, plate, and cone configurations, while also accounting for surface tension gradients, Joule heating, and permeability of the medium. Sadiya et al. [22] analysed the simultaneous effects of these parameters on the flow behaviour of a ternary nanofluid moving through a porous medium over a rotating and stretching surface. Qureshi et al. [23] conducted a machine-learning-based analysis of MHD radiative ternary hybrid nanofluid flow, comprising multi-walled carbon nanotubes (MWCNTs) and Au/Ag nanoparticles suspended in blood, over a porous stretching sheet.

A thorough examination of existing literature demonstrates that the mixed convection flow of a chemically reactive $Al_2O_3 – Cu/H_2O$ hybrid nanofluid over wedge and cone geometries, considering the simultaneous influence of heat generation (absorption) and chemical reaction effects, remains uninvestigated. Aiming to address this gap, the present analysis explores the governing factors of heat and mass transfer in the flow system and builds upon the study of Yahaya et al. [3] by introducing heat generation within the boundary layer. The novelty of this study lies in its numerical assessment of how thermal and solutal Grashof numbers, together with heat generation (absorption) and chemical reaction factors, affect the behaviour of the hybrid nanoliquid over non-isothermal and non-isosolutal wedge and cone surfaces. A comparative evaluation between the two geometries is carried out to highlight the influence of the selected physical elements. This problem is tackled using the BVP5C numerical solver. Graphical representations are used to illustrate the influence of key variables, and tables are provided to report skin friction, mass and heat transmission rates for chosen parameter values. The results show strong consistency and offer valuable insights into the transport phenomena involved.

2. Mathematical modelling

This research presents a numerical exploration of steady-state, laminar, 2D incompressible mixed convective flow of a chemically reactive hybrid nanofluid composed of $Al_2O_3 – Cu/H_2O$ over vertical non-isothermal and non-isosolutal cone and wedge configurations, accounting for the impact of heat generation or absorption. Initially, a nanofluid is prepared by scattering copper (Cu) nanoparticles into water (H_2O), the basic fluid, with the volume fraction represented by ϕ_1. This $Cu – H_2O$ nanofluid is then further modified into a hybrid nanofluid, $Al_2O_3 – Cu/H_2O$, by incorporating aluminium oxide (Al_2O_3) nanoparticles, known for their superior thermal conductivity at a designated volume fraction ϕ_2. This study assumes that the nanoparticles are uniformly shaped and sized and that thermal equilibrium exists between the basic liquids and the suspended nanoparticles.

Figure 1 demonstrates the configuration and co-ordinate system for the 2D flow scenario, here the x–axis runs along the surface area of the cone or wedge and the y–axis is oriented perpendicular to it. The stretched velocity of the surface is defined as $u_w = v_f x/l^2$, and the liquid occupies the area $y \geq 0$. The surface temperature distribution is modelled as $T_w(x) = T_\infty + ax^{s_1}$, while the nanoparticle concentration at the surface is given by $C_w(x) = C_\infty + bx^{s_2}$, with the exponents s_1 and s_2 governing the spatial variation of temperature and concentration, respectively. A value of $s_1 = 0$ represents a surface with constant temperature (isothermal), and $s_2 = 0$ indicates a surface with uniform nanoparticle concentration (isosolutal). The cone or wedge is characterised by a half-angle α, with its radius defined as $r = x \sin\alpha$.

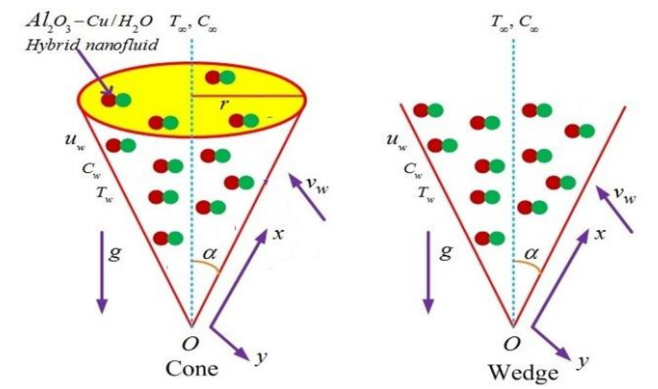


Fig. 1. Flow configuration schematic representation.

The two geometric configurations, cone and wedge, are distinguished using the following criteria:

i) for $\alpha \neq 0$ and $n = 0$, the structure corresponds to a wedge,

ii) for $\alpha \neq 0$ and $n = 1$, the configuration represents a cone.

Taking into account the aforementioned suppositions, the equations that govern this flow problem are established as follows [1,3,5,24]:

$$\frac{\partial}{\partial x}(r^n u) + \frac{\partial}{\partial y}(r^n v) = 0, \tag{1}$$

$$u\frac{\partial u}{\partial x} + v\frac{\partial u}{\partial y} = \frac{\mu_{hnf}}{\rho_{hnf}}\frac{\partial^2 u}{\partial y^2} + g\,[\beta_T(T - T_\infty) + \beta_c(C - C_\infty)]\cos\alpha, \tag{2}$$

$$u\frac{\partial T}{\partial x} + v\frac{\partial T}{\partial y} = \frac{k_{hnf}}{(\rho\, C_p)_{hnf}}\frac{\partial^2 T}{\partial y^2} - \frac{1}{(\rho\, C_p)_{hnf}}\frac{\partial q_r}{\partial y} + \frac{Q^*}{(\rho\, C_p)_{hnf}}(T - T_\infty), \tag{3}$$

$$u\frac{\partial C}{\partial x} + v\frac{\partial C}{\partial y} = D_{hnf}\frac{\partial^2 C}{\partial y^2} - K^*(C - C_\infty). \tag{4}$$

The corresponding boundary constraints [3,5] are:

at $y = 0$:

$$u = u_w,\ v = v_w,\ -k_{hnf}\frac{\partial T}{\partial y} = h_f(T_w - T),\ C = C_w, \tag{5a}$$

as $y \longrightarrow \infty$

$$u \longrightarrow 0, \quad T \longrightarrow T_\infty, \quad C \longrightarrow C_\infty. \tag{5b}$$

To simplify the analysis, the following similarity transformations are introduced [1,3]:

$$\eta = \frac{y}{l}, \quad u = \left(\frac{\nu_f x}{l^2}\right) f'(\eta),$$

$$v = -\left(\frac{\nu_f}{l}\right)(1+n) f(\eta), \quad \theta(\eta) = \frac{T - T_\infty}{T_w - T_\infty}, \tag{6}$$

$$\phi(\eta) = \frac{C - C_\infty}{C_w - C_\infty}.$$

Upon applying the similarity parameters defined by Eq. (6) to the governing Eqs. (1) to (4), it is observed that Eq. (1) is naturally satisfied, while Eqs. (2)–(4) are simplified to the non-linear ODEs shown below:

$$R_1 f''' + R_2(1+n) f f'' - R_2 f'^2 + R_2(\mathrm{Gr}\theta + \mathrm{Gc}\phi)\cos\alpha = 0, \tag{7}$$

$$\left(R_4 + \frac{4}{3}Rd\right)\theta'' + \mathrm{Pr}\,Q\,\theta + \mathrm{Pr}R_3(1+n) f\theta' - s_1 \mathrm{Pr} R_3 f'\theta = 0, \tag{8}$$

$$\phi'' + \frac{\mathrm{Sc}}{R_5}[(1+n) f\phi' - s_2 f'\phi - Rc\phi] = 0. \tag{9}$$

Here:

$$R_1 = \frac{\mu_{hnf}}{\mu_f},\ R_2 = \frac{\rho_{hnf}}{\rho_f},\ R_3 = \frac{(\rho C_p)_{hnf}}{(\rho C_p)_f},\ R_4 = \frac{k_{hnf}}{k_f},\ R_5 = \frac{D_{hnf}}{D_f}.$$

The corresponding boundary constraints are transformed to:

$$f'(0) = \phi(0) = 1, \quad f(0) = S\frac{1}{1+n}, \quad \theta'(0) = -\mathrm{Bi}\frac{(1-\theta(0))}{R_4},$$

$$f'(\infty) = \phi(\infty) = \theta(\infty) = 0. \tag{10}$$

Dimensionless quantities utilised in the governing equations are defined as follows [1,3,5,25]:

- thermal Grashof number: $\mathrm{Gr} = \frac{l^2 g \beta_T (T_w - T_\infty)}{\nu_f u_w}$,
- mass Grashof number: $\mathrm{Gc} = \frac{l^2 g \beta_C (C_w - C_\infty)}{\nu_f u_w}$,
- heat generation/absorption: $S = -\frac{l v_w}{\nu_f}$ ($S > 0$ indicating suction and $S < 0$ indicating injection),
- Biot number: $\mathrm{Bi} = \frac{h_f l}{k_f}$,
- Schmidt number: $\mathrm{Sc} = \frac{\nu_f}{D_f}$,
- chemical reaction parameter: $Rc = \frac{K^* l^2}{\nu_f}$.

As per Rosseland's [26] diffusion estimate, the radiative heat flux q_r is formulated in the following manner, as outlined in references [27–29]:

$$q_r = -\frac{4}{3}\frac{\sigma^*}{k^*}\frac{\partial T^4}{\partial y}.$$

The factors k^* and σ^* designate the mean absorption coefficient and Stefan–Boltzmann constant respectively. By applying a Taylor's series extension to T^4 around the ambient temperature T_∞ and avoiding higher order terms, the expression streamlines to: $T^4 \approx 4\,T_\infty{}^3 T - 3\,T_\infty{}^4$.

Physical and thermal characterisations of the basic liquid H_2O and nanoparticles Al_2O_3, Cu, along with those of the hybrid nanofluid Al_2O_3 – Cu/H_2O, are presented in Tables 1 and 2 given below.

Table 1. Al_2O_3, Cu and H_2O thermo-physical properties [33,34].

Properties	Cu	Al_2O_3	H_2O
C_p, J/(kg K)	385	765	4179
ρ, kg/m³	8933	3970	997.1
k, W/(m K)	400	40	0.613
Pr			6.2

Table 2. Al_2O_3 – Cu/H_2O hybrid nanoliquid thermo-physical properties [1,5,30–32].

Properties	Al_2O_3 – Cu/H_2O hybrid nanoliquid
Viscosity (μ)	$\mu_{hnf} = \frac{\mu_f}{(1-\phi_1-\phi_2)^{2.5}}$
Density (ρ)	$\rho_{hnf} = \phi_2\rho_2 + \phi_1\rho_1 + (1-\phi_1-\phi_2)\rho_f$
Heat capacity (ρC_p)	$(\rho C_p)_{hnf} = \phi_2(\rho C_p)_2 + \phi_1(\rho C_p)_1 + (1-\phi_1-\phi_2)(\rho C_p)_f$
Thermal conductivity (k)	$\frac{k_{hnf}}{k_f} = \frac{\frac{\phi_2 k_2+\phi_1 k_1}{\phi_2+\phi_1} + 2k_f + 2(\phi_2 k_2+\phi_1 k_1) - 2(\phi_2+\phi_1)k_f}{\frac{\phi_2 k_2+\phi_1 k_1}{\phi_2+\phi_1} + 2k_f - (\phi_2 k_2+\phi_1 k_1) + (\phi_2+\phi_1)k_f}$
Diffusion coefficient (D)	$D_{hnf} = (1-\phi_1-\phi_2)D_f$

The key physical quantities appropriate to the current problem are discussed as follows:

$$C_f = \frac{\mu_{hnf}}{\rho_f u_w^2}\left(\frac{\partial u}{\partial y}\right)_{y=0}, \tag{11a}$$

$$\mathrm{Nu}_x = \frac{-x}{k_f(T_w-T_\infty)}\left[\left(k_{hnf}\frac{\partial T}{\partial y}\right)_{y=0} - (q_r)_{y=0}\right], \tag{11b}$$

$$\mathrm{Sh}_x = \frac{-x}{D_B(C_w-C_\infty)}\left(\frac{\partial C}{\partial y}\right)_{y=0}. \tag{11c}$$

Substituting the similarity variables defined in Eq. (6) into Eq. (11) yields the non-dimensional forms of the physical quantities, as presented below:

$$\mathrm{Re}_x^{1/2} C_f = R_1 f''(0), \tag{12a}$$

$$\mathrm{Re}_x^{-1/2}\mathrm{Nu}_x = -\left(R_4 + \frac{4}{3}Rd\right)\theta'(0), \tag{12b}$$

$$\mathrm{Re}_x^{-1/2}\mathrm{Sh}_x = -\phi'(0). \tag{12c}$$

3. Method of solution

The system of Eqs. (7) to (9), along with the corresponding boundary constraints, is solved numerically by utilising the BVP5C solver available in MATLAB. To implement this method, all higher-order differential equations (DEs) are first reduced to a set of first-order equations. The formulation of the problem and procedural flow of the BVP5C technique are illustrated in Fig. 2.

Let:

$$f = y_1,\quad \frac{df}{d\eta} = \frac{dy_1}{d\eta} = y_2,\quad \frac{d^2f}{d\eta^2} = \frac{dy_2}{d\eta} = y_3,\quad \frac{d^3f}{d\eta^3} = \frac{dy_3}{d\eta}, \tag{13}$$

$$\theta = y_4,\quad \frac{d\theta}{d\eta} = \frac{dy_4}{d\eta} = y_5,\quad \frac{d^2\theta}{d\eta^2} = \frac{dy_5}{d\eta}, \tag{14}$$

$$\phi = y_6,\quad \frac{d\phi}{d\eta} = \frac{dy_6}{d\eta} = y_7,\quad \frac{d^2\phi}{d\eta^2} = \frac{dy_7}{d\eta}. \tag{15}$$

Substitution of Eqs. (13)–(15) into Eqs. (7)–(9) yields the transformed equations given below:

$$R_1\frac{dy_3}{d\eta} + R_2(1+n)y_1y_3 - R_2{y_2}^2 + \\ +R_2(\mathrm{Gr}\,y_4 + \mathrm{Gc}\,y_6)\cos\alpha = 0, \tag{16}$$

$$\left(R_4 + \frac{4}{3}Rd\right)\frac{dy_5}{d\eta} + \\ +\mathrm{Pr}(Q\,y_4 + R_3(1+n)y_1y_5 - s_1R_3y_2y_4) = 0, \tag{17}$$

$$\frac{dy_7}{d\eta} + \frac{\mathrm{Sc}}{R_5}[(1+n)y_1y_7 - s_2y_2y_6 - Rc\,y_6] = 0, \tag{18}$$

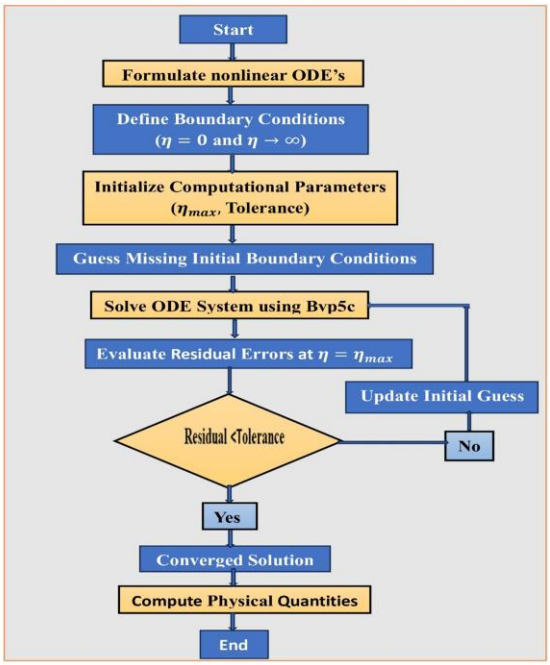


Fig. 2. Iterative BVP5C solution flowchart.

along with the boundary constraints:

$$y_1(0) = \frac{S}{1+n},\quad y_2(0) = y_6(0) = 1,$$

$$y_5(0) = -\frac{\mathrm{Bi}(1-y_4(0))}{R_4}, \tag{19}$$

$$y_2(\infty) = y_4(\infty) = y_6(\infty) = 0, \tag{20}$$

$$\frac{dy_3}{d\eta} = \frac{-R_2(1+n)y_1y_3 + R_2{y_2}^2 - R_2(\mathrm{Gr}\,y_4 + \mathrm{Gc}\,y_6)\cos\alpha}{R_1}, \tag{21}$$

$$\frac{dy_5}{d\eta} = \frac{-\mathrm{Pr}(Qy_4 + R_3(1+n)y_1y_5 - s_1R_3y_2y_4)}{\left(R_4 + \frac{4}{3}Rd\right)}, \tag{22}$$

$$\frac{dy_7}{d\eta} = -\frac{\mathrm{Sc}}{R_5}[(1+n)y_1y_7 - s_2y_2y_6 - Rc\,y_6]. \tag{23}$$

The BVP5C solver generates a solution that is continuous and possesses a continuous first-order derivative over the interval [0, ∞]. Equations (19)–(23) are programmed in MATLAB, and their solutions are obtained using the BVP5C routine. This approach ensures that the convergence criteria are adequately met 10^{-6}.

4. Results and discussion

This section presents graphical illustrations of the temperature $\theta(\eta)$, velocity $f'(\eta)$ and concentration $\phi(\eta)$ distributions for the

hybrid nanofluid Al_2O_3 – Cu/H_2O flowing over a vertical, non-isothermal and non-isosolutal, penetrable wedge and cone. A comparative assessment of the cone and wedge geometries is carried out to evaluate how the leading governing factors impact the flow, temperature and concentration characteristics. The influence of various factors, such as thermal Grashof number Gr, mass Grashof number Gc, heat absorption or generation parameter Q, radiation parameter Rd, Schmidt number Sc, chemical reaction parameter Rc, Biot number Bi, and suction parameter S, on these distributions is analysed and discussed. To explore the physical performance of the structure, the boundary value problem stated in Eqs. (16)–(20) is solved utilising MATLAB's BVP5C solver. The results are provided in both graphical and tabular representations to provide a comprehensive understanding of the underlying physical mechanism. A detailed investigation has been conducted on the skin friction coefficient, Sherwood number and Nusselt number with respect to the major influencing parameters.

The effect of thermal Grashof number, ranging between $1 \le \mathrm{Gr} \le 8$, on $f'(\eta)$, $\theta(\eta)$ and $\phi(\eta)$ distributions of Al_2O_3 – Cu/H_2O hybrid nanoliquid flowing over a wedge and cone is presented in Figs. 3 to 5.

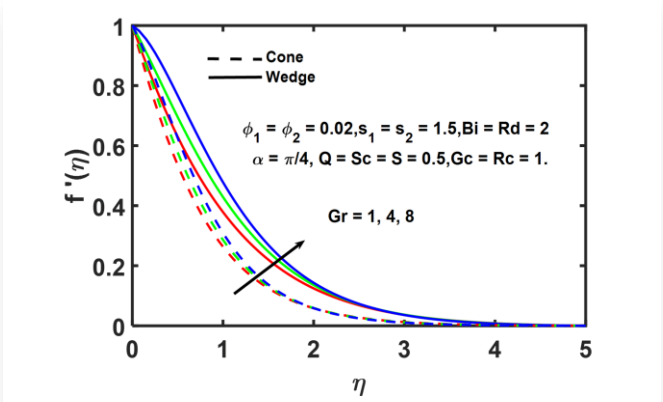


Fig. 3. Thermal Grashof number's effect on velocity profile.

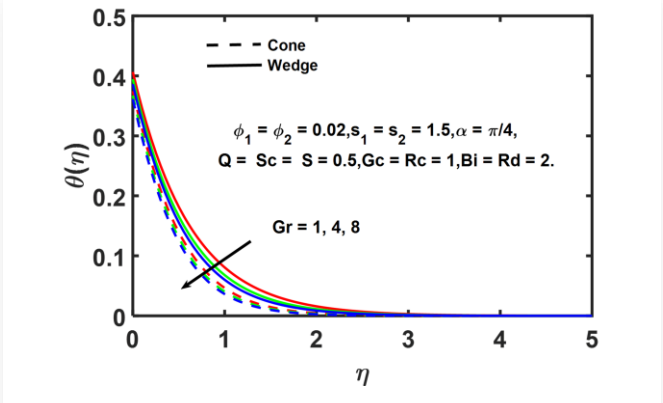


Fig. 4. Thermal Grashof number's effect on temperature profile.

As the values of Gr increase, the velocity distribution rises, while the temperature and concentration distributions exhibit a decreasing tendency. An increase in Gr reduces the boundary layer thickness due to stronger buoyancy forces generated by temperature transformations. This enhances the liquid motion and raises the velocity distribution. This increased acceleration promotes more effective mixing and advection, resulting in a dilution phenomenon that reduces solute concentration. As a result, the concentration boundary layer becomes thinner, further diminishing the concentration distribution. In addition, larger temperature gradients produce stronger buoyant forces, which enhance convective heat transfer. This intensified convection helps dissipate heat more efficiently, thereby reducing the liquid's temperature. The impact is more pronounced for the wedge compared to the cone.

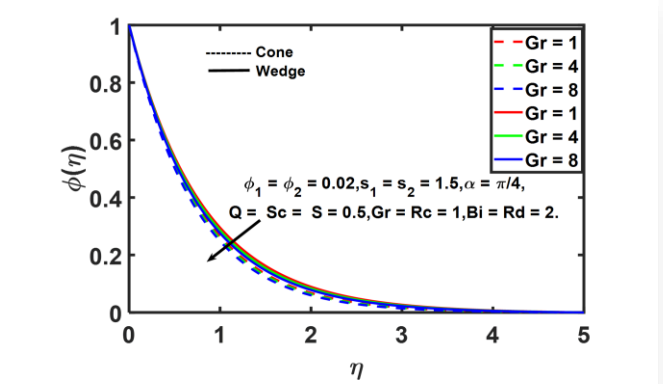


Fig. 5.Thermal Grashof number's effect on concentration profile.

Figures 6 to 8 depict the influence of the mass Grashof number, ranging between $0.1 \le \mathrm{Gc} \le 0.9$, on $f'(\eta)$, $\theta(\eta)$ and $\phi(\eta)$ profiles for both wedge and cone configurations. In a manner similar to Gr, increasing Gc enhances the $f'(\eta)$ profile, whereas $\theta(\eta)$ and $\phi(\eta)$ profiles show a decreasing trend.

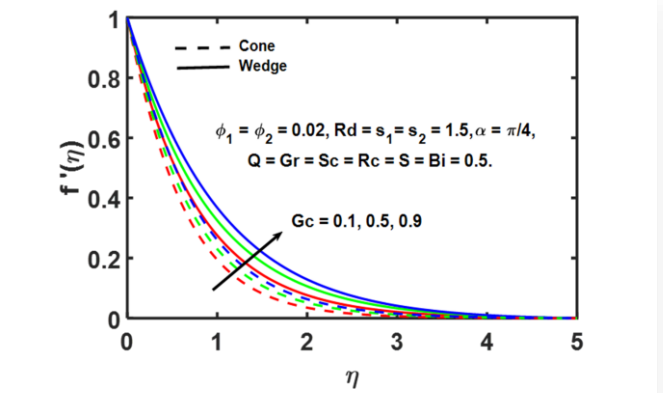


Fig. 6. Mass Grashof number's effect on velocity profile.

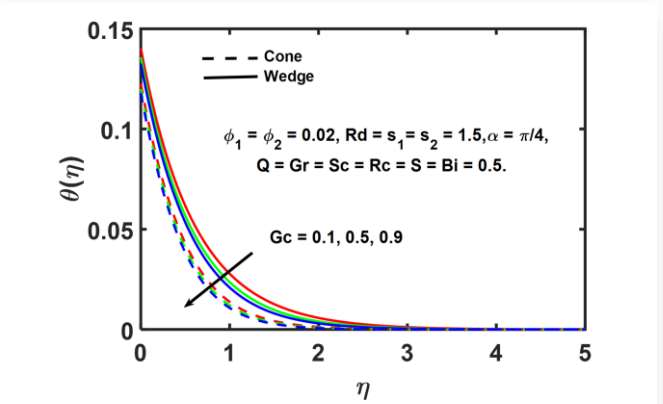


Fig. 7. Mass Grashof number's effect on temperature profile.

This phenomenon arises because the mass Grashof number is directly associated with buoyancy forces; as Gc rises, buoyancy effects become more significant, thereby accelerating the fluid flow. It is also witnessed that the impact of Gc is more pronounced for the wedge compared to the cone in all three profiles.

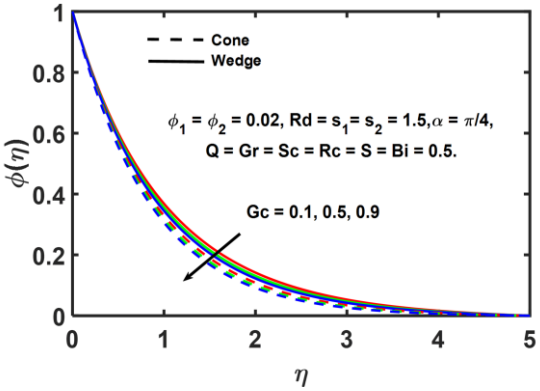


Fig. 8. Mass Grashof number's effect on concentration profile.

Figure 9 illustrates the variation in the $\theta(\eta)$ profile with cumulative values of the radiation parameter, within the range $1 \le Rd \le 2$, for both the wedge and cone. It is noted that as Rd increases, the temperature distribution in the $Al_2O_3 - Cu/H_2O$ hybrid nanofluid rises for both geometries. This occurs because a higher Rd indicates greater thermal radiation, which contributes additional energy to the fluid. Accordingly, more heat is absorbed by the hybrid nanofluid particles, leading to a thicker thermal boundary layer and an elevated temperature profile.

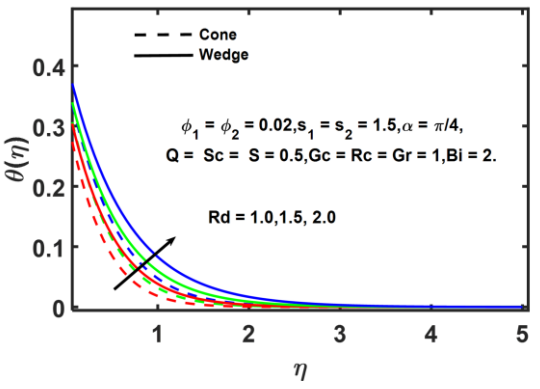


Fig. 9. Thermal radiation parameter's influence on temperature profile.

Figure 10 illustrates the effect of increasing the heat generation parameter, within the range $1.1 \le Q \le 1.3$, on the $\theta(\eta)$ profile for both the wedge and cone geometries. As Q increases, more thermal energy is transferred to the hybrid nanofluid, leading to a rise in stored internal energy within the liquid particles. This results in a thicker boundary layer and a corresponding rise in the temperature profile.

Figure 11 presents the variation of the temperature profile $\theta(\eta)$ of the hybrid nanoliquid with respect to changes in the wall temperature parameter $1 \le s_1 \le 2$, for both wedge and cone geometries. It is evident that $\theta(\eta)$ reduces with the increasing s_1 value. This reduction is due to the strong influence of higher s_1 values on the thermal boundary layer, which becomes thinner, resulting in a lower temperature distribution. Among these three parameters, their effects on $\theta(\eta)$ are found to be more important in the case of the wedge compared to that of the cone.

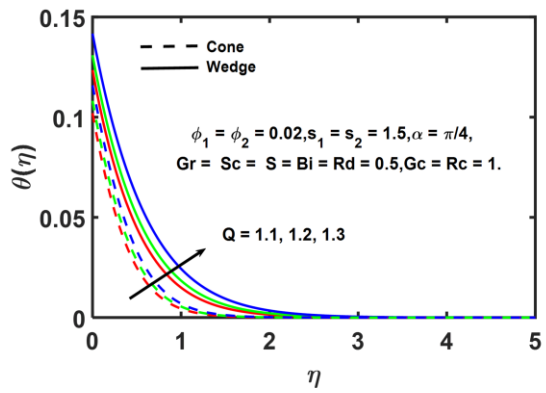


Fig. 10. Heat source factor's influence on temperature profile.

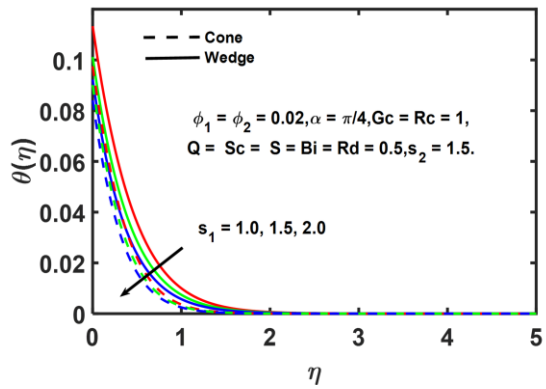


Fig. 11. Wall temperature parameter's influence on temperature profile.

Figures 12 to 14 demonstrate the influence of the chemical reaction factor ($1 \le c \le 3$), Schmidt number ($2 \le Sc \le 4$), and wall concentration parameter ($1 \le s_2 \le 3$) on the $\phi(\eta)$ profile for both the wedge and cone. The plots reveal a consistent decline in $\phi(\eta)$ with the increasing values of Rc, Sc and s_2. This behaviour is attributed to the inverse relationship between viscosity and the chemical reaction rate; an increase in Rc results in a reduction of both viscosity and concentration distribution. Similarly, a rise in Sc implies a decrease in the molecular diffusivity of the liquid, which in turn diminishes the concentration levels within the boundary layer. Regarding the wall concentration factor, as s_2 upsurges, the boundary layer becomes thinner, leading to a decrease in the concentration profile. In all these three cases, the decrease in $\phi(\eta)$ is more pronounced for the cone configuration than for the wedge.

Figures 15 to 17 present the impact of the suction factor within the range $1 \le S \le 2$ on $f'(\eta)$, $\theta(\eta)$ and $\phi(\eta)$ profiles for both cone and wedge. As S increases, all three profiles exhibit a downward trend. This behaviour is attributed to the stronger suction drawing liquid toward the surface, which modifies the boundary layer and reduces the fluid velocity. The inward pull of the fluid lessens surface friction, thereby increasing the rate of heat transfer and resulting in a decreased $\theta(\eta)$ distribution. Suction also eliminates low-energy fluid near the surface, effect-

tively drawing the hybrid nanoliquid closer to the wedge or cone surfaces. The decline in $f'(\eta)$, $\theta(\eta)$ and $\phi(\eta)$ is more significant in the case of the cone than in the wedge.

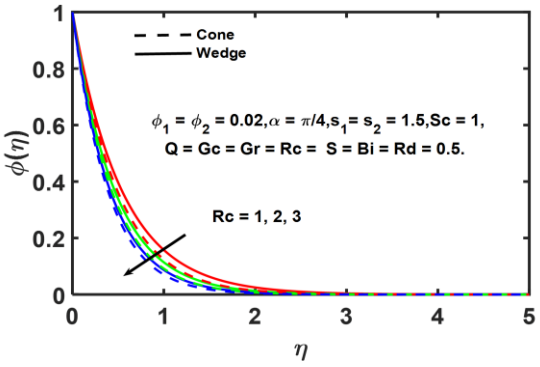


Fig. 12. Chemical reaction parameter's effect on concentration profile.

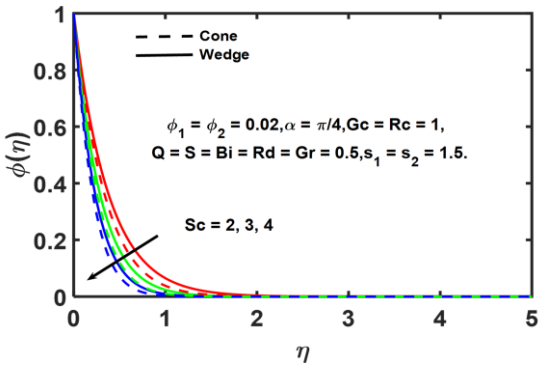


Fig. 13. Schmidt quantity's effect on concentration profile.

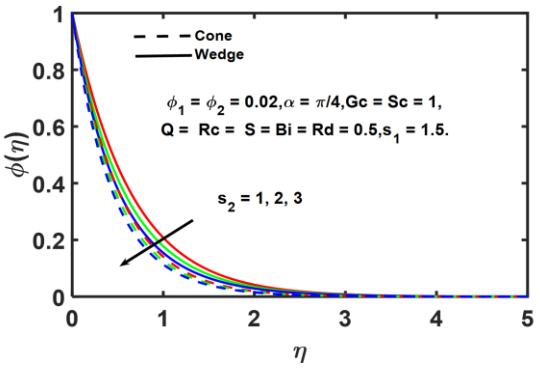


Fig. 14. Wall concentration parameter's effect on concentration profile.

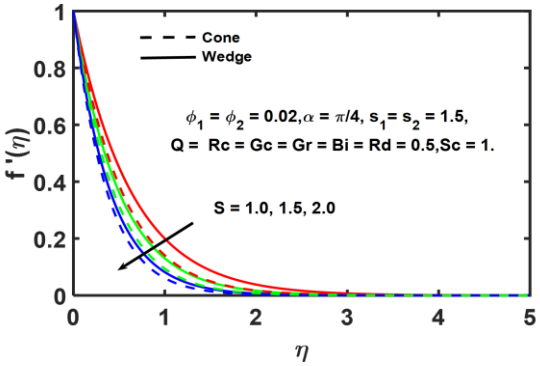


Fig. 15. Suction factor's influence on velocity profile.

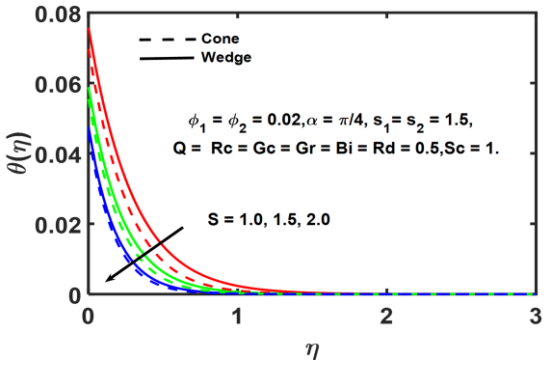


Fig. 16. Suction factor's influence on temperature profile.

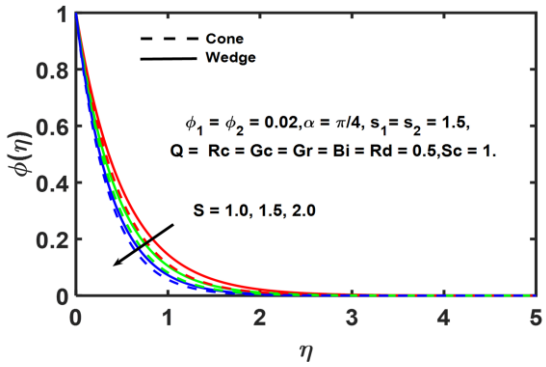


Fig. 17. Suction factor's influence on concentration profile.

Figure 18 illustrates the effect of Biot number, ranging between $1 \leq \mathrm{Bi} \leq 2$, on the $\theta(\eta)$ profile for both the cone and wedge. Bi represents the ratio of convective heat transfer at the surface to conductive heat transfer within the surface. An increase in Bi indicates stronger convective heat exchange between the cone and wedge surface and the neighbouring hybrid nanofluid. As a result, $\theta(\eta)$ increases, leading to a thicker thermal boundary layer. This influence is more important in the wedge configuration than in the case of the cone.

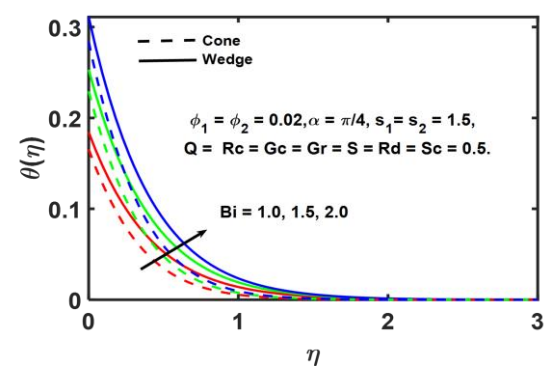


Fig. 18. Biot number's influence on the temperature profile.

Tables 3 and 4 demonstrate the effects of Gr, Gc, *Rd*, *Q*, Sc and *Rc* on the skin friction coefficient C_f, Nusselt number Nu_x and Sherwood number Sh_x for the hybrid nanofluid $Al_2O_3 - Cu/H_2O$ over both cone and wedge geometries. The computations are carried out with fixed values: $\phi_1 = \phi_2 = 0.02$, $\alpha = \pi/4$, $s_1 = s_2 = 1$, Sc = 0.2, *Rd* = *Q* = Gr = Gc = *Rc* = *S* =

Table 3.Influences of Gr, Gc, *Rd*, *Q*, Sc and *Rc* on C_f and Nu_x for both the cone and wedge.

Gr	Gc	*Rd*	*Q*	Sc	*Rc*	C_f		Nu_x	
						Cone	Wedge	Cone	Wedge
0.1						−1.411734	−1.176412	0.616064	0.605640
0.2						−1.409805	−1.173662	0.616071	0.605653
0.3						−1.407876	−1.170915	0.616077	0.605667
0.4						−1.405948	−1.168170	0.616083	0.605681
	0.1					−1.642275	−1.420108	0.614557	0.603147
	0.4					−1.460673	−1.226097	0.615756	0.605161
	0.7					−1.294884	−1.048459	0.616690	0.606633
	1.0					−1.139337	−0.881631	0.617470	0.607814
		1.0				−1.400719	−1.160468	0.765981	0.749786
		1.5				−1.397266	−1.155199	0.911128	0.887971
		2.0				−1.393672	−1.149638	1.051824	1.020541
		2.5				−1.389945	−1.143819	1.188288	1.147751
			0.1			−1.405233	−1.167917	0.621241	0.614034
			0.2			−1.404964	−1.167401	0.620081	0.612257
			0.3			−1.404675	−1.166823	0.618843	0.610299
			0.4			−1.404361	−1.166172	0.617516	0.608127
				0.2		−1.404021	−1.165427	0.616090	0.605693
				0.3		−1.441769	−1.199960	0.615791	0.605267
				0.4		−1.470497	−1.227122	0.615558	0.604919
				0.5		−1.492936	−1.249013	0.615375	0.604632
					0.5	−1.404021	−1.165427	0.616090	0.605693
					0.6	−1.408361	−1.170228	0.616056	0.605635
					0.7	−1.412498	−1.174799	0.616024	0.605580
					0.8	−1.416448	−1.179155	0.615993	0.605527

Table 4. Influences of Gr, Gc, *Rd*, *Q*, Sc and *Rc* on Sh_x for both the cone and wedge.

Gr	Gc	*Rd*	*Q*	Sc	*Rc*	Sh_x	
						Cone	Wedge
0.1						0.606284	0.571215
0.2						0.606336	0.571292
0.3						0.606387	0.571368
0.4						0.606439	0.571445
	0.1					0.582707	0.550370
	0.4					0.601217	0.566799
	0.7					0.616125	0.580182
	1.0					0.628864	0.591689
		1.0				0.606641	0.571756
		1.5				0.606824	0.572047
		2.0				0.607042	0.572397
		2.5				0.607293	0.572802
			0.1			0.606447	0.571426
			0.2			0.606456	0.571445
			0.3			0.606467	0.571467
			0.4			0.606478	0.571492
				0.2		0.606491	0.571521
				0.3		0.773045	0.721728
				0.4		0.925505	0.858809
				0.5		1.067523	0.986330
					0.5	0.606491	0.571521
					0.6	0.625225	0.590917
					0.7	0.643397	0.609699
					0.8	0.661046	0.627916

Bi = 0.5. Note that when evaluating the impact of a specific parameter, all other parameters are kept constant to isolate its effect on C_f, Nu_x and Sh_x.

Tables 3 and 4 indicate that an increase in Gr from 0.1 to 0.4 leads to a slight rise in C_f, Nu_x and Sh_x for both cone and wedge configurations. For the cone, these values are increased by approximately 0.4%, 0.003% and 0.03%, respectively, while for the wedge, the corresponding increases are about 0.7%, 0.006% and 0.04%. When Gc is increased from 0.1 to 1.0, noticeable enhancements are observed. For the cone, C_f, Nu_x and Sh_x increase by approximately 31%, 0.5% and 8%, respectively, while for the wedge, the corresponding increases are about 38%, 0.8% and 8%. As *Rd* increases from 1.0 to 2.5, the cone configuration shows increases of approximately 0.8% in C_f, 55% in Nu_x and 0.1% in Sh_x. For the wedge, the corresponding increases are about 1.4%, 53% and 0.2%, respectively. As *Q* increases from 0.1 to 0.4, both C_f and Sh_x exhibit slight increases by 0.06% and 0.01%, respectively, for the cone and by 0.15% and 0.01% for the wedge. In contrast, Nu_x decreases by 0.6% for the cone and 1% for the wedge. As $0.2 \leq Sc \leq 0.5$, both C_f and Nu_x decrease by 6% and 0.1% for the cone and by 7% and 0.2% for the wedge, respectively. In contrast, Sh_x shows a substantial increase of 76% for the cone and 73% for the wedge. Lastly, increasing *Rc* from 0.5 to 0.8 results in slight reductions in C_f and Nu_x by 0.9% and 0.02% for the cone, and by 1.18% and 0.03% for the wedge. Meanwhile, Sh_x increases by 9% for the cone and 10% for the wedge.

To ensure the validity of the present model, Tables 5 and 6, along with the bar diagrams shown in Figs. 19 and 20, present the computed values of $-f''(0)$ and $-\theta'(0)$ for the specific case when $\phi_1 = 0.00001$ and all other parameters ϕ_2, *Rd*, s_2, *Q*, Gr, Gc, Sc and *Rc* are set to zero, with $Bi = 10^6$. The outcomes demonstrate strong agreement with the existing results reported

in [3,35,36] for the cone configuration, thereby supporting the accuracy of the present formulation.

Table 5.Validation of $-f''(0)$ against existing results for a wedge.

Pr	α	s_1	S	$-f''(0)$		
				Hassanien et al. [35]	Yahaya et al. [3]	Present results
6.2	1	1	1	1.618034	1.61803	1.618281
			0.5	1.280777	1.28078	1.281515
			−0.5	0.780781	0.78078	0.782412
			0	1.00000	1.00001	1.001396

Table 6.Validation of $-\theta'(0)$ against existing results for a wedge.

Pr	α	s_1	S	$-\theta'(0)$		
				Waini et al. [36]	Yahaya et al. [3]	Present results
1	0	0	0	0.5820	0.58201	0.582013
		1		1.0000	1.00001	1.000011
		2		1.3333	1.33333	1.333333
0.72		1		0.8086	0.80864	0.808645

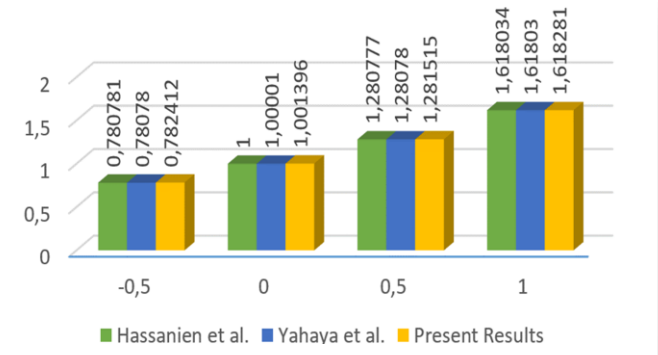


Fig. 19. Comparison of $-f''(0)$ for different values of S.

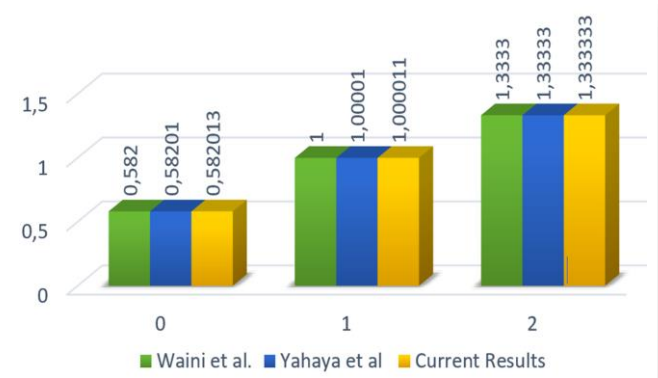


Fig. 20. Comparison of $-\theta'(0)$ for different values of s_1.

5. Conclusions

This work presents a mathematical model for analysing the steady, laminar, two-dimensional mixed convective flow of a chemically reactive hybrid nanoliquid consisting of $Al_2O_3 - Cu/H_2O$ over vertical non-isothermal/non-isosolutal wedge and cone surfaces, incorporating the influence of the heat generation factor. The nonlinear ODE system is numerically solved using MATLAB's BVP-5C solver. The key findings derived from this analysis are outlined below:

- As the values of Gr increase, an enhancement in the velocity profile is observed, whereas both concentration and temperature profiles tend to decline. A similar performance is noted for Gc as well.
- Rising values of Rd, Q and Bi leads to a rise in the temperature distribution of the hybrid nanoliquid for both geometries, whereas an opposite behaviour is noticed with the rise in s_1.
- A consistent decline in $\phi(\eta)$ is observed with increasing values of *Rc*, Sc and s_2. With an increase in S, all three profiles $f'(\eta)$, $\theta(\eta)$ and $\phi(\eta)$ show a decreasing trend.
- An increase in Gr, Gc, *Rd* and Q leads to a rise in the skin friction coefficient, whereas *Rc* produces a contrasting effect. The rate of heat transfer, represented by the Nusselt number, improves with higher Gr, Gc and *Rd* but declines as Q and *Rc* increase. Moreover, the Sherwood number is observed to increase with growing values of Gr, Gc, *Rd*, Q and *Rc* for cone and wedge geometries.

References

[1] Dawar, A., Shah, Z., Tassaddiq, A., Kumam, P., Islam, S., & Khan, W. (2021). A convective flow of Williamson nanofluid through cone and wedge with non-isothermal and non-isosolutal conditions: a revised Buongiorno model. *Case Studies in Thermal Engineering*, 24, 100689. doi: 10.1016/j.csite.2021.100869

[2] Kumar, A., Ray, A.K., Saha, S., Tanwar, D.V., Kumar, B., & Sheremet, M.A. (2023) Flow of hybrid nanomaterial over a wedge: shape factor of nanoparticles impact. *The European Physical Journal Plus*, 138, 901. doi: 10.1140/epjp/s13360-023-04535-8

[3] Yahaya, R.I., Arifin, N.Md., Mustafa, M.S., Pop, I., Ali, F.M., & Mohamed Isa, S.S.P. (2025). Mixed convection hybrid nanofluid flow past a non-isothermal cone and wedge with radiation and convective boundary condition: Heat transfer optimization. *Case Studies in Thermal Engineering*, 66, 105768. doi: 10.1016/j.csite.2025.105768

[4] Sushila, C., Jarwal, V.K., Prasun, C., Loganathan, K., & Pattanaik B. (2024). Mass-Based Hybrid Nanofluid Model for Thermal Radiation Analysis of MHD Flow over a Wedge Embedded in Porous Medium. *Journal of Engineering*, 18, 9528362. doi: 10.1155/2024/9528362

[5] Ramzan, M., Kumam, P., Lone, S.A., Seangwattana, T., Saeed, A., & Galal, A.M. (2023). A theoretical analysis of the ternary hybrid nanofluid flows over a non-isothermal and non-isosolutal multiple geometries. *Heliyon*, 9(4), e14875. doi: 10.1016/j.heliyon.2023.e14875

[6] Reddy, M.V., Ajithkumar, M., Lone, S.A., Ali, F., Lakshminarayana, P., & Saeed, A. (2024). Magneto-Williamson nanofluid flow past a wedge with activation energy: Buongiorno model. *Advances in Mechanical Engineering*, 16(1). doi: 10.1177/16878132231223027

[7] Chandra Reddy, P., Raju, M.C., Raju, G.S.S., & Varma, S.V.K. (2016). Free convective magneto-nanofluid flow past a moving vertical plate in the presence of radiation and thermal diffusion.

Frontiers in Heat and Mass Transfer, 7, 28. doi: 10.5098/hmt.7.28

[8] Mathews, J., & Talla, H. (2024). Unsteady magnetohydrodynamic free convection and heat transfer flow of Al_2O_3 – Cu/water nanofluid over a non-linear stretching sheet in a porous medium. *Archives of Thermodynamics*, 45(1), 165–173. doi: 10.24425/ather.2024.150449

[9] Amit, P., & Shalini, J. (2019). Influence of non-linear chemical reaction on MHD convective flow for maxwell fluid over three different permeable vertical surfaces. *Journal of Nanofluids*, 8, 671–682. doi:10.1166/jon.2019.1639

[10] AL Garalleh, H. (2024). Numerical simulation of heat transport mechanism in chemically influenced ternary hybrid nanofluid flow over a wedge geometry. *Discover Applied Sciences*, 6, 449. doi: 10.1007/s42452-024-06141-4

[11] AI-Arabi, T.H., Mahdy, A., Rashad, A.M., Saad, W., & Nabwey, H.A. (2022). Convective flow of a Williamson hybrid nanofluid in a porous medium through a cone and wedge with the effect of the shape of nanoparticles. *Heat Transfer*, 51(8), 7009−7029. doi: 10.1002/htj.22634

[12] Vajravelu, K., & Nayfeh, J. (1992). Hydromagnetic convection at a cone and a wedge. *International Communications in Heat and Mass Transfer*, 19(5), 701–710. doi: 10.1016/0735-1933(92)90052-J

[13] Rekha, M.B., Sarris, I.E., Madhukesh, J.K., Raghunatha, K.R., & Prasannakumara, B.C. (2022). Activation energy impact on flow of AA7072-AA7075/water based hybrid nanofluid through a cone, wedge and plate. *Micromachines*, 13(2), 302. doi: 10.3390/mi13020302

[14] Chandra Reddy, P., Umamheswar, M., Harinath Reddy, S., Raju, A.B.M., & Raju, M.C. (2022). Numerical study on the parabolic flow of MHD fluid past a vertical plate in a porous medium. *Heat Transfer*, 51(4), 3418−3430. doi: 10.1002/htj.22457

[15] Chandra Reddy, P., Raju, M.C., & Raju, G.C. (2016). Free convective heat and mass transfer flow of heat-generating nanofluid past a vertical moving porous plate in a conducting field. *Special Topics & Reviews in Porous Media: An International Journal*, 7(2), 161−180. doi: 10.1615/SpecialTopicsRevPorousMedia.2016016973

[16] Mathews, J., & Talla, H. (2025). Unsteady magnetohydrodynamic free convection flow of Al_2O_3 – Cu/water nanofluid over a permeable linear stretching sheet through a porous medium with viscous dissipation and heat source/sink. *Journal of Thermal Engineering*, 11(2), 344–356. doi: 10. 14744/thermal.0000919

[17] Ali, R., Iqbal, A., Abbass, T., Arshad, T., & Shahzad, A. (2024). Unsteady flow of silica nanofluid over a stretching cylinder with effects of different shapes of nanoparticles and Joule heating. *Archives of Thermodynamics*, 45(3), 115–126. doi: 10.24425/ather.2024.151222

[18] Ali, R., Mitalipova, A., Ul Hussan, S.W., Kurbanaliev, A., Shahzad, A., & Abduzhabbarov, M. (2025). Shape effects on steady flow and heat transfer of Cu-nanofluid over a nonlinear stretching surface with Joule heating. *Archives of Thermodynamics*, 46(3), 89–104. doi: 10.24425/ather.2025.156581

[19] Shahzad, A., Gulistan, U., Ali, R., Iqbal, I., Benim, A.C., Kamran, M., Ud-Din Khan, S., Ud-Din Khan, S., & Farooq, A. (2020). Numerical study of axisymmetric flow and heat transfer in a liquid film over an unsteady radially stretching surface. *Mathematical Problems in Engineering*, 2020, 1−9. doi: 10.1155/2020/6737243

[20] Zaman, M., Jahan, S., Sohail, M., Farman, M., Nisar., K.S. (2025). Thermal analysis of Williamson nanofluid in cone and wedge geometries: an ANN optimization. *Journal of Thermal Analysis and Calorimetry*, 150, 17413–17435. doi: 10.1007/s10973-025-14658-y

[21] Galal, A.M., Abbas, M., Rajab, A.B., Alsaydi, H.A., Abdallah, S.A.O., Abd EL-Gawaad, N.S., Akgül, A., & Shafique, M. (2022). Simulation of thermally radiative flow of hybrid nanofluid over wedge, plate and cone with elastic-deformation and surface tension gradient. *Journal of Radiation Research and Applied Sciences*, 18(2), 1275−1281, 101396. doi: 10.1016/j.jrras.2025.101396

[22] Sadiya, A.B., & Sucharitha, G. (2025). Computational analysis of MHD ternary hybrid nanofluid flow with thermochemical reactions through a porous medium on a rotating stretching sheet. *Discover Nano*, 20, 168. doi: 10.1186/s11671-025-04353-0

[23] Qureshi, H., Zubair, M., & Altmeyer, S.A. (2025). Machine learning investigation of ternary-hybrid radiative nanofluid over stretching and porous sheet. *Nanomaterials*, 15(19), 1525. doi: 10.3390/nano15191525

[24] Ramana, R.M., Maheswari, Ch., Mohiddin Shaw, S., Dharmaiah, G., Fernandez-Gamiz, U., & Noeiaghdam, S. (2024). Numerical investigation of 3-D rotating hybrid nanofluid Forchheimer flow with radiation absorption over a stretching sheet. *Results in Engineering*, 22, 102019. doi: 10.1016/j.rineng.2024.102019

[25] Raju, K.V., Maheswari, Ch., Ramana, R.M., Varma. S.V., & Raju, M.C. (2026). Comparative numerical study between MHD Forchheimer nano and hybrid nanofluid flows over stretching sheet under aligned magnetic field in the presence of radiation absorption. *International Journal of Modelling and Simulation*, 46(4), 1450–1467. doi: 10.1080/02286203.2024.2393306

[26] Rosseland, S. (1931). *Astrophysik Auf Atomtheoretischer Grundlage*, Springer Berlin Heidelberg. doi: 10.1007/978-3-662-26679-3

[27] Ishak, A. (2010). Thermal boundary layer flow over a stretching sheet in a micropolar fluid with radiation effect. *Meccanica*, 45(3), 367−373. doi: 10.1007/s11012-009-9257-4

[28] Magyari, E., & Pantokratoras, A. (2011). Note on the effect of thermal radiation in the linearized Rosseland approximation on the heat transfer characteristics of various boundary layer flows. *International Communication in Heat and Mass Transfer*, 38(5), 554−556. doi: 10.1016/j.icheatmasstransfer.2011.03.006

[29] Bataller, R.C. (2008). Radiation effects for the Blasius and Sakiadis flows with a convective surface boundary condition. *Applied Mathematics and Computation*, 206(2), 832−840. doi: 10.1016/j.amc.2008.10.001

[30] Sheremet, M., Oztop, H.F., Pop, I., & Al-Salem, K. (2016). MHD free convection in a wavy open porous tall cavity filled with nanofluids under an effect of corner heater. *International Journal of Heat and Mass Transfer*, 103, 955–964. doi: 10.1016/j.ijheatmasstransfer.2016.08.006

[31] Merkin, J.H., Pop, I., Lok, Y.Y., & Grosan, T. (2021). *Similarity Solutions for the Boundary Layer Flow and Heat Transfer of Viscous Fluids, Nanofluids, Porous Media, and Micropolar Fluids*. Elsevier Academic Press. doi: 10.1016/C2019-0-01299-X

[32] Nazir, U., Sohail, M., Hafeez, M.B., & Krawczuk, M. (2021). Significant production of thermal energy in partially ionized hyperbolic tangent material based on ternary hybrid nanomaterials. *Energies*, 14(21), 6911. doi: 10.3390/en14216911

[33] Khashi'ie, N.S., Waini, I., Mukhtar, M.F., Zainal, N.A., Bin Hamzah, K., Arifin, N.M. & Pop, I. (2022). Response surface methodology (RSM) on the hybrid nanofluid flow subject to a vertical and permeable wedge. *Nanomaterials*, 12(22), 4016. doi: 10.3390/nano12224016

[34] Oztop, H.F., & Abu-Nada, E. (2008). Numerical study of natural convection in partially heated rectangular enclosures filled with

nanofluids. *International Journal of Heat Fluid Flow*, 29(5), 1326–1336. doi: 10.1016/j.ijheatfluidflow.2008.04.009

[35] Hassanien, I.A., Abdullah, A.A., & Gorla, R.S.R. (1998). Flow and heat transfer in a power-law fluid over a nonisothermal stretching sheet. *Mathematical and Computer Modeling*, 28(9), 105–116. doi: 10.1016/S0895-7177(98)00148-4

[36] Waini, I., Ishak, A., & Pop, L. (2021). Hybrid nanofluid flow over a permeable non-isothermal shrinking surface. *Mathematics*, 9(5), 538. doi: 10.3390/math9050538